A&A 413, 1019–1028 (2004)
DOI: 10.1051/0004-6361:20031545

Astronomy & Astrophysics

The gamma-ray source LSI +61°303

II. Multiwavelength emission model

D. A. Leahy⋆

Department of Physics, University of Calgary, Calgary, Canada T2N 1N4

Received 2 June 2003 / Accepted 29 September 2003

Abstract. The multi–wavelength spectrum of LSI +61°303 is summarized. The X-ray to γ-ray luminosity of $L_{\rm ic} \simeq 1.5 \times 10^{35}$ erg/s is due to inverse Compton emission from relativistic electrons around a pulsar. The X-ray to γ-ray spectrum determines the electron energy index, which is consistent with the observed radio spectrum if it mainly optically thin. The inverse Compton emission from a compact region of electrons peaks at periastron due to the higher density of stellar photons. This compact region is highly self-absorbed at radio frequencies implying the quiescent radio emission comes from a separate diffuse population of electrons. The number and total energy of electrons in the diffuse region is ∼0.1 of that in the compact region ($\sim 3 \times 10^{43}$ electrons, $\sim 5 \times 10^{38}$ erg). The compact region cannot be static due to its high internal pressure: expansion leading to loss of electrons and injection of new electrons are required. A pulsar with spin period ≃0.1 s can provide sufficient injection power. A steady diffuse outflow of electrons from the compact region produces too much optically thick synchrotron emission. The alternative is bulk expansion of the compact electron bubble, with dynamic pressure limiting the expansion velocity and resulting in expansion away from the Be star. Injection ends as the bubble wall facing the Be star stalls and the pulsar's orbit takes it out of the bubble. Alternately, the Rayleigh-Taylor instability could cause the bubble to break up before the exit of the pulsar. In either case, energy injection rates of $\sim 2\ L_{\rm ic}$ into the bubble result in a detached bubble of size, velocity and electron content similar to the initial conditions used by Peracaula (1997) to model radio outbursts for LSI +61°303.

Key words. stars: neutron – stars: individual: LSI +61°303 – stars: binaries: general – stars: emission line, Be – X-rays: binaries

1. Introduction

LSI +61°303 is an unusual radio emitting X-ray binary system. Paper I (Leahy 2001) gives a review of its properties. Here an abbreviated introduction is given. The radio source LSI +61°303 is highly variable, exhibiting outbursts every 26.496 days which have rise times of ∼1 day and last ∼10 days (Gregory & Taylor 1978; Taylor & Gregory 1982). Two-frequency radio monitoring indicates a flat spectral index, and the emission has been interpreted as optically-thin synchrotron radiation for most of the outburst, with indication that the source becomes self-absorbed for a short time at the beginning of the outburst rise (Taylor & Gregory 1984). VLBI observations show that at its maximum size the emitting region has a dimension of $\sim 5 \times 10^{13}$ cm, and an expansion velocity $(2.0–6.4) \times 10^7$ cm s^{-1} (Massi et al. 1993). The phase of peak flux varies between 0.4–1.0 of the radio ephemeris (phase 0 arbitrarily defined as MJD 43366.275, period equal to 26.496 days), most often occurring at phase ∼0.6 (Paredes et al. 1990; Ray et al. 1997). Distance determinations place LSI +61°303 at 1.8–2.3 kpc (Gregory et al. 1979; Frail & Hjellming 1991).

Optical data show that the primary is a rapidly-rotating star of spectral type B0 V (Hutchings & Crampton 1981) or B0–B0.5 III (Paredes & Figueras 1986). The best determination of orbital period, 26.42 days, and eccentricity, 0.30, comes from RXTE/ASM observations (Leahy 2001). Orbital solutions derived from infrared photometric observations imply high eccentricities (0.7–0.8), with a best-fit periastron passage at radio phase $\phi_{\rm p} = 0.5$ (Marti & Paredes 1995). Infrared measurements imply the presence of a dense equatorial disk, and a mass-loss rate in the wind of $1–4 \times 10^{-7}\ M_\odot$ yr^{-1} has been estimated from these observations assuming an opening angle of 15° for the disk and an initial wind velocity of 5 km s^{-1} (Waters et al. 1988).

Simultaneous X-ray and radio monitoring indicate that the X-ray and radio fluxes are separated by ∼0.4 in orbital phase (Harrison et al. 2000). *ASCA* observations (Leahy et al. 1997), show that the spectrum is described by a relatively hard power-law, and therefore the emission mechanism is non-thermal in nature. Harrison et al. (2000) present RXTE/PCA and RXTE/HEXTE observations which are consistent with a power law spectrum from X-ray to γ-ray. COMPTEL has also detected emission in the 1–10 MeV band from the same region (van Dijk et al. 1994) but the error circle also contains the quasar 4U 0241+61. The RXTE/PCA and RXTE/HEXTE observations by Harrison et al. (2000) resolve LSI +61°303 from the QSO and show that COMPTEL flux is dominated by the QSO and not LSI +61°303.

⋆ e-mail: leahy@iras.ucalgary.ca

In this paper, the X-ray, γ-ray and radio observations are reviewed and a multiwavelength emission model is constructed. This yields a new interpretation of the nature of the physical nature of LSI +61°303.

2. Summary of observations

LSI +61°303 has been observed on numerous occasions in various wavebands from radio through γ–ray. Here the focus is understanding the the relativistic electron population around the compact object in the context of radio, X-ray and γ–ray observations.

The radio observations are summarized in Ray et al. (1997). 2.25 GHz and 8.3 GHz flux and 2.25–8.3 GHz spectral index light curves are given for a ∼13.5 month period, as well as time-averaged flux and spectral index light curves for a 26.69 day radio period. The time-averaged emission has a mean minimum flux of 17 mJy at 8.3 GHz with a 2.25–8.3 GHz spectral index of $\alpha = 0.5$. The peak of emission has a flux of 163 mJy at 8.3 GHz with a spectral index of $\alpha = 0.0$. α is defined here using $f_\nu = f_0 \nu^{-\alpha}$. The radio outburst JD 2 448 840–2 448 860 observed at 4.9 GHz and 1.5 GHz is modelled by an expanding sphere of relativistic electrons by Peracaula (1997). The initial radius and magnetic field are 1.5×10^{13} cm and 0.15 Gauss; the cloud moves radially outward at 1.5×10^9 cm s^{-1} and expands at 3×10^7 cm s^{-1}; electrons are injected over 7 days with energy index 2.1 between energies 10^{-6} erg and 5×10^{-3} erg and with a total number of injected electrons of 2.1×10^{46}. It is apparent that the radio outburst involves large velocities in order to explain the observed size of the radio jet, and that a significant expansion is required in order to explain the radio spectral index variation. The parameters are also given for comparison with what is derived here from the multiwavelength observations.

Optical observations (Hutchings & Crampton 1981) give period, K, e and ω with large uncertainties. Here, binary period and e are taken from the RXTE/ASM analysis above. Marti & Paredes (1995) summarize previous optical observations which indicate the primary star is Be star with $T_{\rm eff} = 22\,500$ K. They then use infrared observations to constrain the nature of the circumstellar disk of material around the primary star. The temperature of the disk was taken to be 17 500 K, then the density of the disk is given by the parameters in Table 1 of that paper.

The X-ray through γ–ray flux measurements are summarized in Harrison et al. (2000). The best measurement of LSI +61°303's X-ray spectrum is by the ASCA satellite (Leahy et al. 1997). The 0.5–10 keV X-ray spectrum has $\alpha = 0.70 \pm 0.07$ and $\alpha = 0.82 \pm 0.07$ in the two ASCA observations. More extensive flux measurements are from ROSAT and RXTE/PCA (Harrison et al. 2000). The mean PCA 2–10 keV flux for 10 pointings is 1.1×10^{-11} erg cm^{-2} s^{-1}, which is higher by a factor 2 than the ASCA 2–10 keV flux. The mean ROSAT 0.5–2 keV flux for 9 pointings is 2×10^{-12} erg cm^{-2} s^{-1}, which is higher by a factor 1.3 than the ASCA 0.5–2 keV flux. Only the ROSAT flux is highly sensitive to the column density to LSI +61°303, which has been determined by the ASCA spectrum (6×10^{21} cm^{-2}). The above indicates that the ASCA flux was from a low flux part of the orbital cycle. The PCA flux is the most representative for the orbital cycle average of LSI +61°303. The EGRET 100 MeV flux is also representative of the orbital cycle average. The PCA–EGRET spectral index, assuming a power law is $\alpha = 0.69$, consistent with the ASCA values but better determined due the wide energy range. Other high energy measurements (>100 keV) are contaminated by a nearby QSO as discussed by Harrison et al. (2000), so are not considered here. The X-ray to γ-ray spectrum (normalization averaged over an orbital cycle) can be integrated to give the total 0.5 keV to 100 MeV luminosity: $L_{\rm ic} = (h\nu f_\nu(100\ {\rm MeV}) - h\nu f_\nu(0.5\ {\rm keV}))(4\pi d^2)/(1-\alpha) = 1.3 \times 10^{35}$ erg/s.

Figure 1 shows the X-ray and γ–ray flux measurements plotted vs. energy. The ASCA data are consistent with coming from a low flux part of the orbital cycle. However the ROSAT data should be representative of the orbital cycle. So there is evidence for a turndown in the spectrum below about 2 keV. Alternately there could be a significantly higher column density (yielding a larger correction to the ROSAT fluxes) that was not detected with ASCA, but this is considered unlikely. A change in the spectral index by 0.5 in spectral index would be expected when adiabatic losses are present. Adiabatic losses, proportional to energy, E, dominate at lower energies and inverse Compton losses, proportional to E^2, dominate at higher energies (e.g. see Longair 1994).

3. Properties of the relativistic electron distribution

Previous studies have determined that the radio emission is synchrotron (e.g. Peracaula 1997) and the X-ray through γ–ray is inverse-Compton emission (e.g. Leahy et al. 1997; Harrison et al. 2000). The RXTE/ASM X-ray light curve (Leahy 2001) is smoothly modulated with a peak at constant orbital phase, which can be modeled by a constant electron population which has variable emission only due to the variation of UV photon flux from the primary star during the elliptical orbit.

The basic model used here for LSI +61°303 is as follows: electrons are accelerated to relativistic energies by a pulsar in orbit around the Be star primary star. A radio pulsar has a rotational energy loss rate of $L_{\rm r} = I * \Omega * {\rm d}\Omega/{\rm d}t$ which for $I = 1.1 \times 10^{45}$ gm cm^2, $P = 1$ s and ${\rm d}P/{\rm d}t = 1 \times 10^{-14}$ gives $L_{\rm r} = 4 \times 10^{32}$ erg/s. However $L_{\rm r}$ goes as $1/P^3$ so $P = 0.1$ s gives $L_{\rm r} = 4 \times 10^{35}$ erg/s. Normal radio pulsars range in P from 0.1 to 2 s and in ${\rm d}P/{\rm d}t$ from a few 10^{-12} to 10^{-17}. The required spin-down luminosity for LSI +61°303 is $L_{\rm r} = L_{\rm ic}/(\epsilon_{\rm rp}\epsilon_{\rm ic})$ where $\epsilon_{\rm rp}$ is the efficiency of converting spin-down power into relativistic particles and $\epsilon_{\rm ic}$ is the fraction of power in newly created relativistic particles converted into inverse-Compton radiation. E.g. taking $\epsilon_{\rm rp} = 0.9$ and $\epsilon_{\rm ic} = 0.36$ gives $L_{\rm r} = 4 \times 10^{35}$ erg/s. This is attained or exceeded by a small but significant fraction (∼2%) of normal radio pulsars (the younger ones). The spin-down age of a pulsar sufficient to power LSI +61°303 ($P = 0.1$ s, ${\rm d}P/{\rm d}t = 1 \times 10^{-14}$), for a braking index of 3, is 1.6×10^7 yrs.

The acceleration mechanism could be electromagnetic fields in the vicinity of the pulsar or shock acceleration at the boundary of the pulsar outflow and the stellar wind from the primary. The flux of stellar photons interacts with the

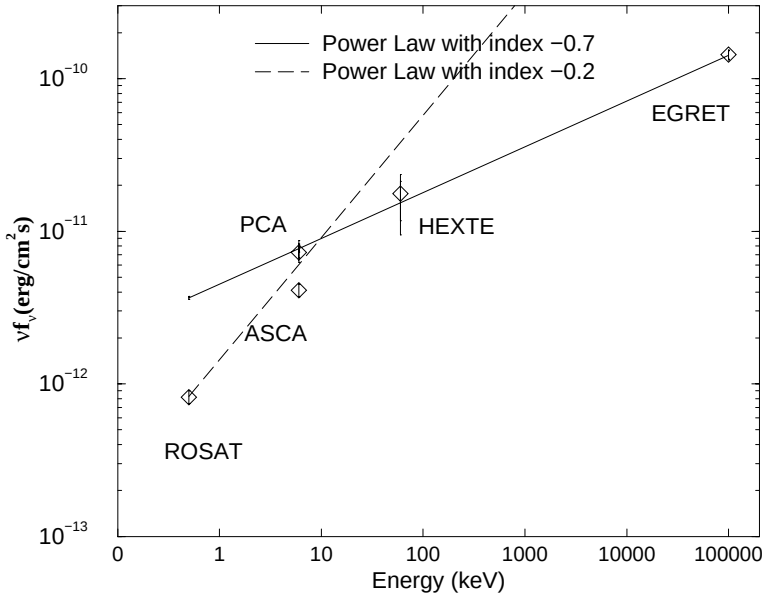

Fig. 1. νf_ν vs. energy from ROSAT, ASCA, RXTE/PCA, RXTE/HEXTE and EGRET, and power-law fit to PCA and EGRET values. A separate power-law with index changed by 0.5 can fit the ROSAT data as well (see text).

Table 1. Binary system parameters.

$P_{\rm bin}$	$26.42d$	e	0.28	D	2.0 kpc
M_1	$10\,M_\odot$	T_1	26 500 K	L_1	1.3×10^{38} erg/s
M_2	$1.4\,M_\odot$	P_2	0.1s	B_2	10^{12} G
a	5.8×10^{12} cm				

power law distribution of relativistic electrons to produce a broad power law distribution of photons from X-ray through γ-ray energies. Due to the magnetic field in the vicinity of the pulsar, the same electrons radiate synchrotron photons in the 1 GHz to 200 GHz range. The average energy of stellar photons is $E_{\rm s} = 2.7kT = 6.1$ eV with the stellar temperature $T = 26\,500$ K (taken between the Johnson 1963, and the Schmidt-Kaler 1982, values for T for a B0V star). For a magnetic field B in the synchrotron emitting region, electrons of energy $E_{\rm e} = (\nu/(6.266\times10^{18}\ {\rm Hz}(B/{\rm Gauss})))^{0.5}$ radiate at frequency ν. For example, electrons at $E_{\rm e} = 1.26\times10^{-5}$ erg radiate at $\nu = 1$ GHz and at $E_{\rm e} = 1.79\times10^{-4}$ erg radiate at $\nu = 200$ GHz for $B = 1$ Gauss. These same electrons produce inverse-Compton photons of energy $E_{\rm IC} = 4(E_{\rm e}/(m_{\rm e}c^2))^2E_{\rm s}/3$ of 1.96 keV and 392 keV.

The eccentric orbit of the pulsar and its associated relativistic electron cloud result in the moderate modulation of the X-ray through γ-ray flux. The radio outburst is much more highly variable in intensity than the X-ray. It does not occur at the same orbital phase from cycle to cycle, but evidence indicates that on average the radio peak follows periastron by ~0.4 in orbital phase. The radio outburst is due to a rapidly expanding cloud of relativistic electrons.

The constraints on the relativistic electron populations are considered next. The parameters of the binary system are summarized in Table 1 and other parameters of the emission model are described below.

3.1. Inverse-Compton emitting electron population

There is evidence, from the X-ray light curve, for a steady population, which is responsible for the X-ray to γ–ray emission. There must also be an outburst population, which is drawn from the steady population and responsible for radio outburst. The steady population is considered first.

The X-ray through γ–ray emission is inverse-Compton emission from a steady population of relativistic electrons in a small region around the compact object, called the compact cloud here. The power law emission from 0.5 keV to 100 MeV implies an electron population with energy spectrum index 2.38 over an electron energy range of 6.4×10^{-6} erg to 2.9×10^{-3} erg. The electron energy index is determined more reliably from the X-ray through γ–ray emission than the radio emission since the synchrotron emission is complicated by optical depth effects.

The compact object is taken to be a pulsar, i.e. a rotating ($P \sim 0.1$ s) neutron star. The electrons can be accelerated to the upper energy above in the pulsar environment as follows. The magnetosphere electric field at the light cylinder using the dipole approximation is $E_{\rm lc} = cB_{\rm lc} = 2.76\times10^8$ V/m with $B_{\rm lc} = B_{\rm s}(R_{\rm N}/R_{\rm lc}c)^3$ for $P = 0.1$ s and surface magnetic field $B_{\rm s} = 10^{12}$ Gauss. This gives a light cylinder voltage of 1.3×10^{15} V and a maximum electron energy $E_{\rm max}$ of 2.8×10^3 erg. Fermi shock acceleration in the outflow gives a maximum electron energy of $E_{\rm max} = (3/20)u_1{}^2eBt_{\rm acc} = 7\times10^{-3}$ erg with $u_1 \simeq 440$ km s^{-1} the shock velocity, $B \simeq 1$ Gauss the magnetic field in the acceleration region, and $t_{\rm acc}$ the

acceleration time. $t_{acc} = t_{ic}(E) = (m_e c^2)^2/(3\sigma_T c U_s E/4) =$ 1500 s is limited by the inverse-Compton loss time for electrons (with $E = 1.8 \times 10^9$ eV) which produce by inverse-Compton the highest energy (100 MeV) photons. σ_T is the Thomson cross-section and $U_s = L_s/(4\pi a^2) = 10$ erg/cm^3 is the energy density of stellar photons, with L_s is the stellar blue luminosity and $a = 5.8 \times 10^{12}$ cm is the semi-major axis for neutron star and stellar masses of 1.4 $M_\odot$ and 10 $M_\odot$. $L_s \simeq 1.3 \times 10^{38}$ erg/s is derived from the absolute V magnitude (−4.3) and a bolometric correction of −2.27 for spectral type B0 (from Johnson 1963). For comparison, Schmidt-Kaler (1982) gives $L_s = 2.0 \times 10^{38}$ erg/s for a B0V star.

The electron number distribution is a power law in energy: $N(E_e) = N_0(E_e/m_e)^{-\gamma}$ with energy index related to the inverse-Compton powerlaw index by $\gamma = 2\alpha + 1 = 2.38$ and $N_0 = n_0 V$ with n_0 the electron density per unit electron energy, and V the emitting volume. N_0 is determined by comparing the theoretical inverse-Compton flux: $f_{IC}(E) = 2.1 \times 10^{41}(N_0/d^2)(R_s/a)^3(T_s/K)^3(E/h)(2.1 \times 10^{10}(T_s/K)(h/E))^{(\gamma-1)/2}$ erg cm^{-2} s^{-1} with the observed inverse-Compton flux at any energy, such as 100 MeV. In the above, d is the distance to LSI +61°303, taken as 2 kpc (Frail & Hjellming 1991). Integrating this over energy from $E_1 = 6.4 \times 10^{-6}$ erg (which produce 0.5 keV X-rays) to $E_2 = 2.8 \times 10^{-3}$ erg (which produce 100 MeV γ-rays) gives number of emitting electrons: $N_{IC} = \int_{E_1}^{E_2} N(E)\mathrm{d}E/m_e = 2.6 \times 10^{43}$. The total energy is given by: $E_{IC} = \int_{E_1}^{E_2} N(E)E\mathrm{d}E/m_e = 5.3 \times 10^{38}$ erg. The inverse Compton lifetime of the electrons is in the range 1.5×10^3 s to 6.9×10^5 s, much shorter than synchrotron loss times, which range from 900 days to 11 000 days.

3.2. Quiescent synchrotron emitting electron population

The radio spectral index data (e.g. Ray et al. 1997) shows that spectral index is approximately constant over the radio phase interval 0.8 to 0.2, which is binary phase ≃0.6 to 1.0. This phase interval is refered to as the quiescent radio phase, whereas the outburst radio phase interval (discussed below) is binary phase ≃0 to 0.6.

The electron energy range giving the radio emission is $1.5 \times 10^{-5} B^{-0.5}$ erg for 1.46 GHz to $1.8 \times 10^{-4} B^{-0.5}$ erg for 200 GHz, with B the magnetic field in Gauss. The synchrotron spectrum should have the same index as the X-ray to γ–ray spectrum if it is optically thin. The radio $\alpha \simeq 0.5$ is close to the X-ray to γ–ray $\alpha = 0.69$. The difference could be explained by a small admixture of optically thick synchrotron emission.

The normalization of the radio spectrum depends on the number of radio emitting electrons and the magnetic field. The electron number distribution function (e.g. Lang 1974) is: $N(E) = K(\gamma)(E_T/\mathrm{erg}^2)(E/\mathrm{erg})^{-\gamma}$ with $K(\gamma) = (2-\gamma)/((E_2/\mathrm{erg})^{2-\gamma} - (E_1/\mathrm{erg})^{2-\gamma})$, so $K(\gamma) = 8.24 \times 10^{-3}$ for E_1 and E_2 corresponding to 1 and 200 GHz, and E_T the total electron energy integrated over energies $E_1 < E < E_2$. Then the synchrotron flux density is given by: $F_{syn}(\nu) = 0.93 \times 10^{-23}\alpha(\gamma)K(\gamma)(E_T/\mathrm{erg})(\mathrm{cm}^2/d^2)(B/\mathrm{Gauss})^{(\gamma+1)/2}(6.26 \times 10^{18}/\nu)^{(\gamma-1)/2}$ erg/(cm^2 s Hz) with $\alpha(\gamma) = 2^{(\gamma-3)/2}((\gamma+7/3)/(\gamma+1))\Gamma((3\gamma-1)/12)\Gamma((3\gamma+7)/12) = 1.802$. For a field of 1 Gauss, and a flux of ∼17 mJy at 8.3 GHz (for the radio phase interval 0.8 to 0.2) the number of radio emitting electrons is 9.0×10^{41}, and the total energy in the radio emitting electrons is 3.5×10^{37} erg. That this is much less than the number of inverse-Compton emitting electrons is a further argument for separate emission regions.

The total electron energy in the same energy range E_1 to E_2, corresponding to 1 to 200 GHz synchrotron, derived from the X-ray to γ–ray spectrum is 2.9×10^{38} erg, a factor 8.3 larger. This may be due to: i) the magnetic field is smaller than 1 Gauss (thus requiring more energy and a larger number of radio emitting electrons); or ii) the majority of the inverse Compton emitting electrons are in a high density region (the compact cloud) and the majority of the radio emitting electrons are in a low density region (the diffuse cloud). For the first case where there is only one region, the compact cloud, a magnetic field of 0.3 Gauss yields identical electron populations derived from synchrotron and inverse Compton mechanisms and a total energy in the radio emitting energy range of 2.0×10^{38} erg.

However the synchrotron emission is self absorbed unless the size is large. The self-absorption frequency is given by: $\nu_s = 34 \times 10^6$ Hz $(S(\nu_s)/1000$ mJy$)^{0.4}(B/\mathrm{Gauss})^{0.2}(\theta/\mathrm{arcsec})^{-0.8}$. ν_s increases for smaller size or larger flux. Below the self-absorption frequency the spectrum turns over to have a positive spectral index of 2.5. A self-absorption frequency above ∼1.4 GHz is ruled out by radio observations. Figure 2 illustrates the dependence of the self-absorption frequency on the diameter of the emitting region, in units of the semimajor axis, a, for a few cases of interest. The electron distribution with energy index, γ_e, is assumed to be 2.38. For the steady (minimum) radio emission, a flux of $S_1 = 20$ mJy at 5 GHz is taken for illustration, and for peak of outburst a flux of $S_1 = 200$ mJy at 5 GHz is taken. The magnetic field, B, is taken to be a decreasing function of size, with the value B_1 equal to the field at size $0.01a$, with two cases illustrated: $p = 1$ has B decreasing as 1/size and $p = 3$ has B decreasing as 1/size^3. The former is appropriate for a azimuthal wind flow field and the latter for a fixed dipole field. The self-absorption frequency depends strongly on size but weakly on the other parameters: as $(S_1 B_1^{0.5})$ to a power depending on γ_e. Thus the quiescent electron population must come from a region larger than $\gtrsim 3a$.

Thus the only consistent situation is the existence of two regions: a compact region of size $\lesssim a/10$ (to be consistent with the inverse-Compton orbital modulation); and a diffuse region of size $\gtrsim 3a$. The compact region emits the bulk of the inverse-Compton photons since the stellar seed photon density goes as $1/r^2$. The compact region is synchrotron-optically thick over the observed radio band, thus emits very little flux. The lack of a significant self-absorbed component in the radio spectrum limits the size of the compact region observationally. Since a self-absorbed synchrotron spectrum is not seen during quiescence, limiting the self-absorbed flux to less than 2 mJy at 8.3 GHz yields an upper size limit of $0.032a$. The diffuse region is optically thin and emits almost all of the radio synchrotron photons. The compact region will emit an optically thick synchrotron spectrum, with positive spectral index of 2.5 below the self-absorption frequency. One can take 1.7 mJy at 8.3 GHz (10% of the observed flux) as the upper limit of flux from the

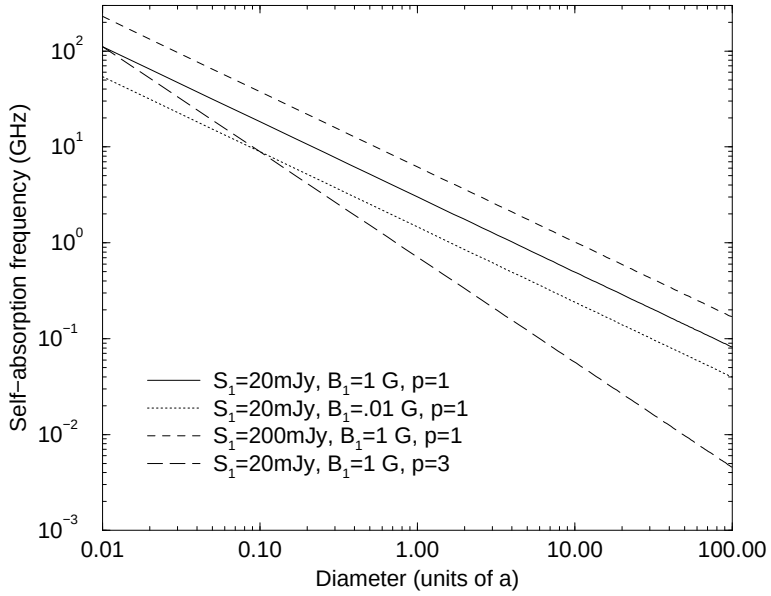

Fig. 2. Self-absorption frequency vs. diameter of the emitting region, for different cases (see text).

compact region, of radius R_c. Then the upper limit on radius is $R_c/a < 0.03B^{1/4}$, with B in Gauss. To avoid self-absorption, the diffuse region must have a size of a few times a: for 0.01 Gauss the lower limit is $\simeq 1.2a$ and for 1 Gauss the lower limit is $\simeq 3.5a$ (see Fig. 2). These sizes are consistent with either: a constant leakage of electrons from the compact region, or remnant electrons from previous outbursts.

In summary, there should be an extended region in the binary system, with a small but significant fraction of the total electron population, which is responsible for the quiescent radio emission in the system. The compact region around the pulsar can contain the majority of the electrons and produce most of the inverse Compton emission but will be optically thick to radio synchrotron emission and make a small contribution to the observed radio emission.

3.3. The confinement problem for the compact region

Here are considered confinement mechanisms for the compact region. The pressure of the compact region is due to the relativistic electrons: $P_c = E_t/(3V_c) = 2.1 \times 10^1\,\mathrm{Nm}^{-2}$, with E_t the total electron energy, derived from the inverse-Compton emission, and V_c the volume of the compact region, taken as a sphere of size $0.1a$ for illustration. Using circumstellar disk parameters from Waters et al. (1988), the thermal pressure is: $P_{th}(r) = \rho_o(r/10\ R_\odot)^{-3.2}kT_w/(\mu m_p) = 1.2 \times 10^{-3}\,\mathrm{Nm}^{-2}$. Here $\rho_o = 10^{-11}$ gm cm^{-3}, $T_w = 17\,500$ K, $\mu = 1.3$ and P_{th} is evaluated at $r = a$. The thermal pressure in the circumstellar disk is insufficient: the pressure balance of relativistic electrons with thermal pressure at the pulsar orbit yields $R_c \simeq 4a$. This implies no confinement since thermal pressure is rapidly decreasing with distance from the primary. The dynamic pressure from the ram pressure of the circumstellar disk on the moving compact region is given by $P_d(r) = \rho_o(r/10\,R_\odot)^{-3.2}v^2 = 2.9{\times}10^{-1}\,\mathrm{Nm}^{-2}$. Here v is the relative velocity of the compact region boundary and the circumstellar disk material, estimated by using the pulsar orbital velocity at $r = a$. It is larger than thermal pressure by a factor of 130 (at apastron) to 280 (at periastron).

An application of balance of dynamic and relativistic electron pressure using spherical symmetry yields $R_c \simeq r_{orb}/2$ with r_{orb} the instantaneous orbital radius of the pulsar from the primary. However, the dynamic pressure vanishes on the trailing half of the compact region. Magnetic pressure can provide confinement if there is a magnetic field, B_{ex}, in the circumstellar disk. To obtain $R_c < 0.1a$, one requires $B_{ex} > 73$ Gauss at r_{orb}. However the existence of a circumstellar disk normally implies that the thermal pressure exceeds the magnetic pressure, or that $B_{ex} < 0.55$ Gauss at $r_{orb} = a$. Thus outflow from, or expansion of, the compact region is expected.

3.4. Outflow from the compact region

An outflow solves the confinement problem by allowing a significant fraction of the electrons (and thus internal pressure) to escape the compact region in a steady manner. This can occur by numerous small volumes (blobs) which break off from the compact region and expand individually into the circumstellar environment. Inverse-Compton losses dominate so the diffusion loss equation takes the form: $\mathrm{d}N(E,t) = \mathrm{d}/\mathrm{d}E(a_{ic}E^2N(E))$ with $a_{ic} = 4\sigma_T c U_{rad}/(2m_e{}^2c^4)$ is the inverse-Compton loss coefficient and U_{rad} is the energy density of stellar photons. The initial condition is $N(E,0) = KE^{-p}$, yielding the solution for the case of a independent of t: $N(E,t) = KE^{-p}(1 - Eat)^{-(2-p)}$. Since the inverse-Compton losses in a blob flowing away at velocity v from the B star are variable and dropping rapidly with time, the flow time (or distance) for a given energy electron in a single blob is found by integrating: $-\mathrm{d}E/\mathrm{d}t = a_{ic}(t)E^2$ with $a_{ic}(t) = a_{ic}(r_o)r_o{}^2/(r_o + vt)^2$. This gives $1/E = a_{ic}(r_o)r_o t_f/(r_o + vt_f)$ for the flow time t_f at energy E. The flow distance at energy E is $x_f = vt_f = v/(Ea_{ic}(r_o)(1 - v/Ea_{ic}(r_o)r_o))$, leading to a

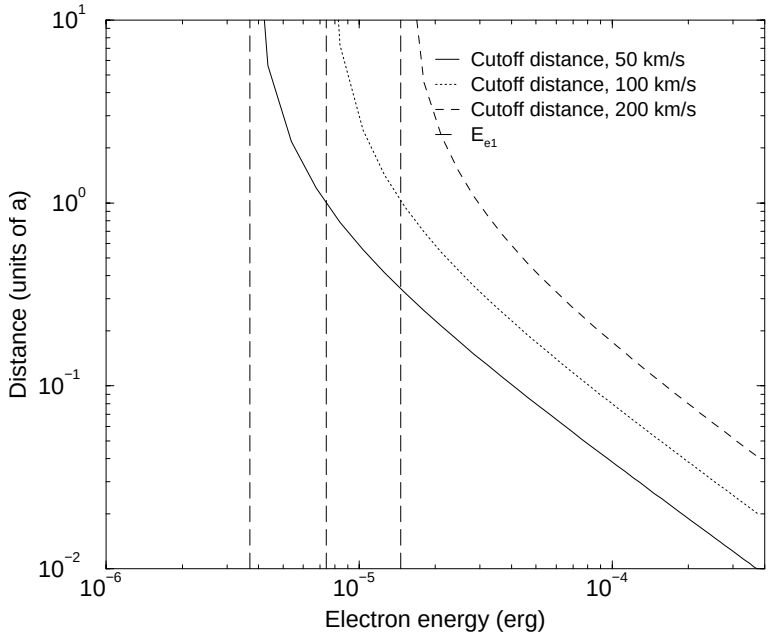

Fig. 3. Cutoff distance vs. electron energy, for flow velocities of 50, 100 and 200 km s^{-1} (see text).

cutoff energy, $E_{\rm cut} = v/a_{\rm ic}(r_{\rm o})r_{\rm o}$, below which electrons survive with little losses.

If the flow was responsible for the radio outburst the velocity would need to be as high as $v = s/t_{\rm rad} = 1100$ km s^{-1}, using a size $s = 8.2a$ and timescale of 5 days (e.g. Massi et al. 1993). However the outburst is a transient event and the steady outflow velocity, v, is limited by dynamic pressure (given earlier). The internal pressure in the electron flow is given by $P_{\rm cf} = E_{\rm t} * f/(3V_{\rm f})$ with f the fraction of the total electron energy that is in the flow and $V_{\rm f}$ the volume occupied by the flow. The resulting flow velocities, for $r_{\rm o} = a$, a spherical flow volume of radius $0.4a$, and $f = 0.1$, 0.5 and 0.9 are 55, 122 and 164 km s^{-1}. Figure 3 shows the cutoff distance vs. energy for 3 flow velocities, with the cutoff energy indicated by the vertical lines.

In summary, below $E_{\rm cut}$, which depends on the flow velocity, the electron spectrum retains a power law form at all distances downstream. Above this energy, the electron spectrum is sharply cutoff with the cutoff energy decreasing with increasing downflow distance, and decreasing to $E_{\rm cut}$ in the limit of large downflow distance.

The net energy spectrum summed over the flow is the same as the injection spectrum for $E < E_{\rm cut}$ and steeper than the injection spectrum by one power of E for electrons with energy $>\simeq 2E_{\rm cut}$. For the no-flow case inverse-Compton losses dominate the full energy range so that the full spectrum is steeper than the injection spectrum by one power of E. Thus the flow electron spectrum is the same as the no-flow spectrum above $>\simeq 2E_{\rm cut}$. This energy range includes all but the lowest energy radio emission and all but the lowest energy X-ray emission. Including adiabatic losses, the energy spectrum is equal to the injection spectrum below the maximum of $E_{\rm cut}$ and the energy below which adiabatic losses dominate.

The flow region is optically thick over the entire range of synchrotron emission giving a size which is a function of electron energy as in Fig. 3. This changes the optically thick spectrum from the usual 2.5 spectral index to a 1.5 index: $F_\nu = \pi S_\nu (r/d)^2$ with size $r = r_{\rm o}(\nu_{\rm o}/\nu)^{0.5}$ from $r = \text{const.} \times 1/E$ and $E = \text{const.} \times \nu^{0.5}$. The observational limit on size of optically thick synchrotron emission at 8.3 GHz (electron energy 3.6×10^{-5} erg) is $\simeq 0.03a$ (given above). This is much smaller than the size of the flow region (Fig. 3) for reasonable flow velocities, ruling out the steady flow model. Thus the alternative of a bulk expansion of the compact region is considered.

3.5. Bulk expansion model

In this case, it is assumed that the compact relativistic electron population remains in a coherent region, and does not mix with the circumstellar medium as it did for the flow model above. The sound speed in the relativistic electron region (called a bubble here) is large ($c/3$) so the interior of the bubble is homogeneous in pressure. The presence of magnetic fields interior to the bubble also contributes to a homogeneous interior pressure. The electron pressure cannot be balanced by the thermal pressure of the circumstellar medium resulting in expansion of the bubble. The neutron star orbit is taken to be in the plane of the circumstellar disk, with disk parameters from Waters et al. (1988). The density of the disk and the bubble expansion velocity determine the dynamic pressure at the boundary. Since the density is not uniform, the expansion velocity of the bubble will be non-uniform: it will be lowest on the side facing the primary star and highest on the side facing away from the primary. The difference in expansion velocity grows as the density contrast increases: the bubble expands asymmetrically.

A bubble expansion model was calculated as follows. Relativistic particles were injected at a constant rate (net, after losses) into the bubble, by the pulsar. The relativistic particle energy, E, inside the bubble increases and drives the bubble expansion by internal pressure $P = E_{\rm t}/3V_{\rm c}$. For the examples

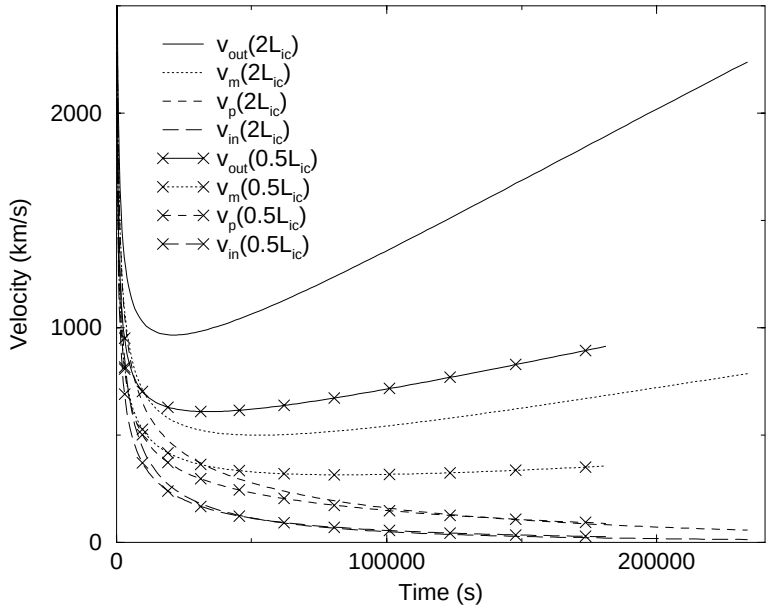

Fig. 4. Expansion velocity of points on the bubble surface: outer point, midway points, point at the pulsar orbit, and inner point, for energy injection rates of $0.5\,L_{\rm ic}$ and $2\,L_{\rm ic}$.

shown here the net injection rates were $2\,L_{\rm ic}$ and $0.5\,L_{\rm ic}$. The initial size of the bubble (which does not affect the results) was taken as a sphere of radius 5×10^9 cm. The external medium was the Be stellar wind disk with density decreasing as $r^{-3.2}$ with r the distance from the Be star and normalization giving a density of 10^{-11} g/cm^3 at $r = 10\,R_\odot$. Thermal pressure of the external medium was ignored as it is much less than dynamic pressure for the times of expansion calculated here.

When the bubble is very small, the expansion and bubble volume, $V_{\rm c} = 4\pi {r_{\rm c}}^3/3$ are spherical, with $r_{\rm c}$ the radius of the bubble. The electron energy, $E_{\rm t}$, increases linearly with time at the net injection rate, $\mathrm{d}E_{\rm t}/\mathrm{d}t$, taken as a constant. The dynamic pressure, $P_{\rm d}$, depends on the expansion velocity, $v = \mathrm{d}r_{\rm c}/\mathrm{d}t$, so pressure balance gives: ${r_{\rm c}}^{3/2}\mathrm{d}r_{\rm c}/\mathrm{d}t = C1t^{1/2}$ with $C1 = (4\pi/3)^{-1/2}(r/10\,R_\odot)^{1.6}(\mathrm{d}E_{\rm t}/\mathrm{d}t/(3\rho_{\rm o}))^{1/2}$ and r the distance from the pulsar to the B star. Since this initial expansion is rapid, r is constant, here taken as the periastron distance for the case of eccentricity of 0.3, $r_{\rm per} = 4.1\times10^{12}$ cm. The solution for $r_{\rm c}$ is: $r_{\rm c}(t) = ({r_{\rm c0}}^{5/2} + C1t^{3/2}5/3)^{2/5}$ with initial value of $r_{\rm c}$ taken as the light-cylinder radius $r_{\rm c0} = cP/2\pi = 4.8\times10^8$ cm. The expansion velocity rapidly increases to a maximum, $\sim5\times10^4$ km s^{-1}, at $\sim$0.05 s and smoothly drops to $\sim4\times10^3$ km s^{-1} at $\sim$65 s, at which time the bubble radius reaches 0.01 of $r_{\rm per}$. At this time the expansion starts to become aspherical, thus the numerical solution was initiated at time 65 s.

The numerical solution for the bubble expansion calculates $r_{\rm c}(t)$ for four different points on the boundary of the bubble: the point at the same distance from the B star as the pulsar, $r_{\rm p}$; the outer and inner points, $r_{\rm out}$ and $r_{\rm in}$ (furthest and closest to the B star); and the point halfway in distance from the B star between inner and outer points, $r_{\rm m}$. The equations solved numerically are: $\mathrm{d}r/\mathrm{d}t = v$ and $v = C2(r)t^{1/2}/{V_{\rm c}(t)}^{1/2}$ with $C2 = (r/10\,R_\odot)^{1.6}(\mathrm{d}E_{\rm t}/\mathrm{d}t/(3\rho_{\rm o}))^{1/2}$ Since the volume of the bubble $V_{\rm c}(t)$ depends on the size and shape of the bubble the solutions for all points on the bubble surface are coupled. To obtain an approximate solution using the four selected points, the bubble volume was taken as volume of an ellipsoid with major axis equal to the difference between inner and outer points and semi-minor axis equal to the distance of the mid-way point to the bubble axis which connects the inner and outer points. Since the bubble expansion velocities decrease with time, time steps were chosen that increase as $t^{0.7}$. The solution above for the initial spherical expansion was used as a starting solution for the numerical solution. The numerical solution was then iterated several times using the solution from the previous iteration for $V_{\rm c}(t)$.

For the examples shown here the final times were taken as a few 10^5 s. The times that the thermal pressure at the inner boundary exceeds internal bubble pressure are 3.2, 3.0 and 2.3$\times$ 10^5 s for $\mathrm{d}E/\mathrm{d}t = 0.5$, 1 and 2 $L_{\rm ic}$. The times that the pulsar overtakes the bubble boundary due to its orbital motion are 1.8, 2.2 and 2.7×10^5 s for $\mathrm{d}E/\mathrm{d}t = 0.5$, 1 and 2 $L_{\rm ic}$.

The results of the calculation are shown in Figs. 4 and 5. Figure 4 shows the growth velocity of the bubble at the 4 selected points vs. time. The velocity drops rapidly at first, but as the outer edge (and mid-way point) move out to lower density regions, they speed up again. Figure 5 shows the distances of the 4 points from the original pulsar position in units of $r_{\rm per}$. Also shown is growth of the bubble volume with time.

3.6. The radio outburst

The expansion of the compact region provides a natural explanation of the radio outbursts. A net energy injection rate of $2\,L_{\rm ic}$ gives a 3 day delay between the initial bubble expansion and the time the outer point of the bubble reaches 2.4 AU. The outer point has velocity 2200 km s^{-1} and the velocity of the center of the bubble is 1100 km s^{-1}. At this time, the pulsar exits the side of the bubble, due to its orbital motion. The bubble then continues to expand without further energy injection. Since it

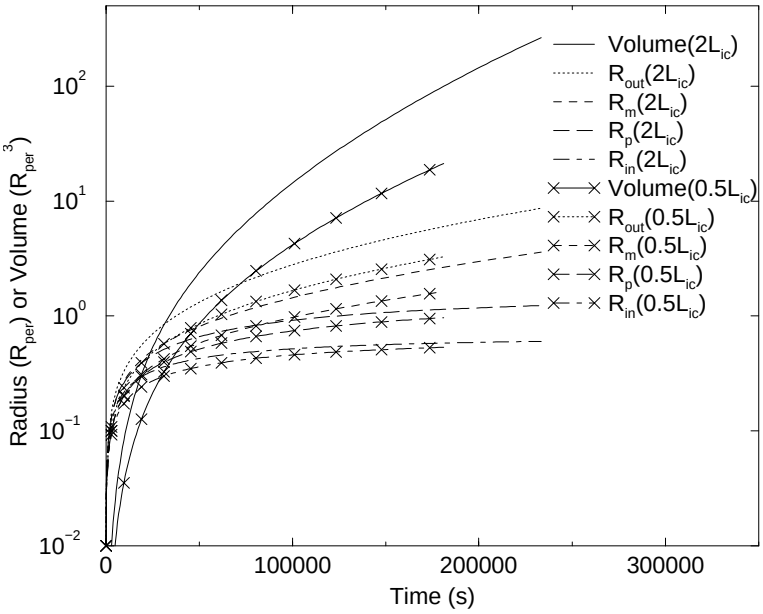

Fig. 5. Distances of points on the bubble surface from the pulsar position, and volume of the bubble, for energy injection rates of $0.5L_{\rm ic}$ and $2L_{\rm ic}$.

is similar to the initial bubble used by Peracaula (1997), the subsequent evolution of the bubble can reproduce the observed radio outbursts (as discussed in that work). A net injection rate of $0.5L_{\rm ic}$ gives ∼2.1 day delay for the outer point to reach 1 AU with velocity 900 km s^{-1}, before the pulsar exits the bubble. The lower injection rate would result in a much smaller radio outburst.

The lack of observed synchrotron self-absorption during outburst puts upper limits on magnetic field. The observed size 2 days after radio outburst peak (Massi et al. 1993), for a distance of 2 kpc, is 8.2a, which rules out B_1 much larger than 1 Gauss. For comparison, the model of Peracaula (1997) uses an initial size of 1.5×10^{13} cm or 2.6a, which applies ∼2 days before outburst peak. Observations of individual cycles (e.g. Ray et al. 1997) show 2.25 GHz outburst emission starting at variable times: from 1 to 5 days prior to outburst peak, with no evidence for self-absorption. The self-absorption frequency curves in Fig. 2 apply to other combinations of S_1 and B_1. For example, the first and last curves also are valid for $S_1 = 200$ mJy and $B_1 = .01$ Gauss, and the second curve for $S_1 = 200$ mJy and $B_1 = .0001$ Gauss. Thus the lack of observed self-absorption above 1.4 GHz is consistent with the observations if $B \lesssim .01$ Gauss 2 days before outburst peak $B \lesssim .001$ Gauss 2 days after peak, for the case of $p = 1$ (wind magnetic field). For the case of $p = 3$ (dipole magnetic field) the upper limits on B are ∼300 times larger.

The rapid expansion of the relativistic electrons is accompanied by adiabatic losses which change the electron spectral index by 1 below the energy, $E_{\rm Ad}$. Below $E_{\rm Ad}$ adiabatic losses dominate and above $E_{\rm Ad}$ inverse Compton and synchrotron losses dominate. Below $E_{\rm Ad}$ the synchrotron or inverse-Compton spectral index is flattened by 0.5. Figure 6 shows the calculated adiabatic break energy for a spherical region with initial size 0.1a starting at distance a from the Be star with initial magnetic field, B, as given, and expanding outward and center moving outward at a constant velocity, $v_{\rm exp}$, of either 500 km s^{-1} or 1000 km s^{-1}. Since the inverse-Compton losses are much larger than synchrotron losses within a few times a of the Be star for LSI +61°303, $E_{\rm Ad}$ is nearly independent of B for reasonable values of B. Whether adiabatic losses affect the radio spectrum is very sensitive to B and the expansion velocity: for $B = 0.01$ Gauss and $v_{\rm exp} = 500$ km s^{-1}, the radio spectrum below ∼5 GHz is affected after 2 days, and prior to 2 days the radio spectrum is affected to much higher frequencies.

The flattening of the spectrum of outburst electrons by 0.5 compared to the quiescent population is seen clearly in the phase averaged observations of 2.25 and 8.3 GHz lightcurves and 2.25–8.3 spectral index (Ray et al. 1997). At peak outburst the spectral index is ≃0.00, flatter by 0.5 than the quiescent spectral index of ≃−0.50. When the flux increases from quiescent (∼20 mJy) to twice that value, one expects an equal admixture of quiescent and outburst radio emission: at that time the observed spectral index is ∼−0.25 equal to the average of quiescent and outburst peak spectral indices.

3.7. Termination of injection

For LSI +61°303, the radio outburst occurs each binary orbit, thus the bubble must separate from the energy injection and subsequently move outward from the binary system. Two possible mechanisms of separation are discussed here.

In the first, the pulsar overtakes the bubble boundary due to its orbital motion. For typical injection rates, the bubble boundary at the pulsar's orbit, $R_{\rm p}$, slows down dramatically at a few 10^4 s. This allows the pulsar (with orbital speed ∼200 km s^{-1}) to overtake the boundary at a time of a few 10^5 s at a relative velocity nearly equal to the orbital velocity. The original bubble, without the energy injection source, continues to expand, lose pressure and move outward. A swept up shell of high density material including compressed magnetic field surrounds the bubble and prevents new energy injection from the pulsar from penetrating the bubble.

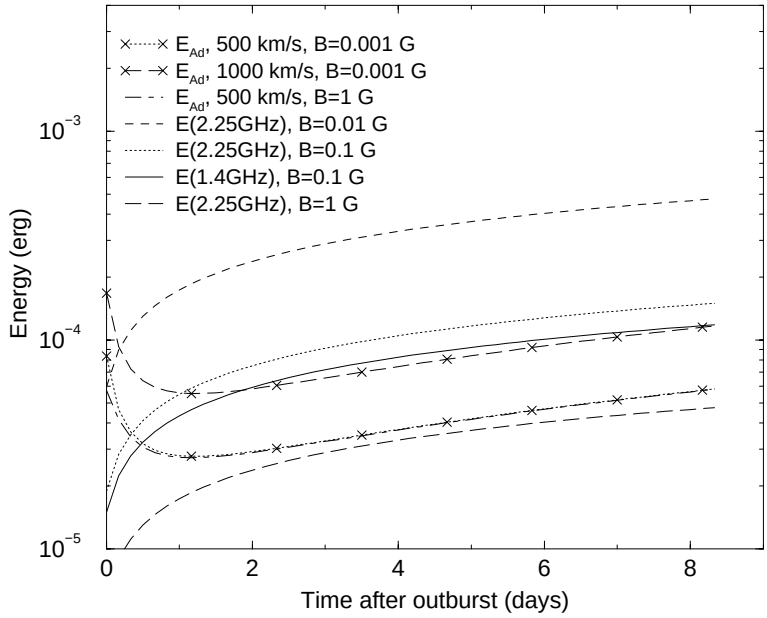

Fig. 6. Electron energy, $E_{\rm Ad}$, below which adiabatic losses dominate for an expanding region, for two cases: expansion velocity of 500 km s^{-1} and 1000 km s^{-1}. Also shown are the electron energies, E(1.4 GHz) and E(2.25 GHz), emitting 1.4 GHz and 2.25 GHz synchrotron, for various initial magnetic fields.

In the second mechanism, the bubble splits due to the Rayleigh-Taylor instability. On the outer side of the bubble, the boundary is accelerating and has a heavy fluid (the swept-up circumstellar disk matter) overlaying a light fluid (the relativistic electrons of the bubble interior). Since the bubble wall is decelerating for points inside the pulsar orbit (see Fig. 4 for $R_{\rm p}$ and $R_{\rm in}$) there is no instability of the bubble wall inside the pulsar orbit. This results in growing indentations of dense bubble wall material which can pinch off the bubble anywhere outside the pulsar orbit. The result is a small bubble (size $< a$) containing the pulsar with energy injection, and a large bubble or several large fragments (size a few times a) without energy injection. The large bubble or fragments continues to expand, lose pressure and move outward. The small bubble can maintain a rapid enough lateral growth rate that the pulsar never needs to overtake its wall.

The radio outburst is essentially the same for either mechanism. The smooth X-ray light curve is more consistent with the second mechanism where there is a compact electron population at all orbital phases. The second mechanism, via the Rayleigh-Taylor instability, would result in more variability in flux and in orbital phase of the radio outbursts.

4. Conclusions

A qualitative model was proposed two decades ago to explain the radio outburst of LSI +61°303 by Maraschi & Treves (1981). The first quantitative model of the radio to γ-ray spectrum was presented by Leahy et al. (1997). That discussion showed that the sub-eV (radio) spectrum should be synchrotron in origin, and the super-eV (X-ray to γ-ray) spectrum should be inverse Compton in origin. It also gave constraints on the magnetic field and relativistic electron populations. Independent of B, for a given electron energy spectral index, the inverse Compton and synchrotron spectra have the same spectral indices. However a given energy of relativistic electrons produces inverse Compton and synchrotron photons of different energies.

From the analysis here, the synchrotron and inverse Compton emission come from two separate populations of electrons: a synchrotron optically thick one near the neutron star producing the inverse-Compton emission and a synchrotron optically thin one producing the synchrotron emission. Relativistic electrons are accelerated in the environment of a pulsar orbiting the primary Be star. Most of the electrons are confined to a small volume and emit inverse Compton X-rays and γ-rays. A small but significant fraction of the total number of relativistic electrons is from previous radio outbursts and is spread out in the binary system. This gives the quiescent radio emission, with spectral index similar to that of the X-rays and γ-rays. Radio outburst occurs due to the expansion of the compact region into the circumstellar disk. The asymmetry in external density results in an asymmetrically expanding bubble of relativistic electrons. Expansion is rapid ($\sim$1000 km s^{-1}) in the outward direction but stalls inside the pulsar orbit. Evidence for adiabatic losses show up in the radio spectrum of the outburst by the observed change in spectral index by 0.5. The energy injection into the outburst population of electrons ends when the expanding bubble detaches from the pulsar, either by orbital motion of the pulsar or by Rayleigh-Taylor instabilities in the bubble wall.

In this paper the existing data on LSI +61°303 was used in the development of a quantitative model for the inverse-Compton emission and synchrotron emission during quiescence and outburst. The model include injection of relativistic particles by a pulsar and subsequent expansion of the resulting bubble. The next step in the study LSI +61°303 is to develop a more detailed numerical simulation of the expansion of the

relativistic electron bubble which includes both the dynamics of the expansion and a calculation of the evolution of the relativistic electron population and magnetic fields interior to the bubble.

Acknowledgements. DAL acknowledges support from the Natural Sciences and Engineering Research Council.

References

Frail, D. A., & Hjellming, R. M. 1991, AJ, 101, 2126
Gregory, P. C., & Taylor, A. R. 1978, Nature, 272, 704
Gregory, P. C., Taylor, A. R., Crampton, D., et al. 1979, AJ, 84, 1030
Harrison, F., Ray, P., Leahy, D., Waltman, E., & Pooley, G. 2000, ApJ, 528, 454
Hutchings, J. B., & Crampton, D. 1981, PASP, 93, 486
Johnson, H. 1963, in Basic astronomical data- Stars and stellar systems III, ed. K. Strand (University of Chicago Press)
Lang, K. 1974, Astrophysical Quantities (New York: Springer-Verlag)
Leahy, D., Harrison, F., & Yoshida, A. 1997, ApJ, 475, 823
Leahy, D. A. 2001, A&A, 380, 516
Longair, M. 1994, High Energy Astrophysics (Cambridge University Press)
Maraschi, L., & Treves, A. 1981, MNRAS, 194, 1P
Marti, J., & Paredes, J. M. 1995, A&A, 269, 249
Massi, M., Paredes, J. M., Estalella, R., & Felli, M. 1993, A&A, 269, 249
Paredes, J. M., Estalella, R., & Rius, A. 1990, A&A, 232, 377
Paredes, J. M., & Figueras, F. 1986, A&A, 154, L30
Peracaula, M. 1997, Ph.D. Thesis, University of Barcelona
Ray, P., Foster, R., Waltman, E., Tavani, M., & Ghigo, F. 1997 ApJ, 491, 381
Schmidt-Kaler, Th. 1982, in Numerical data and Fuctional Relationships in Science and Technology, vol. 2b, ed. K. Schaifers, H. Voigt (Berlin: Springer)
Taylor, A. R., & Gregory, P. C. 1982, ApJ, 255, 210
Taylor, A. R., & Gregory, P. C. 1984, ApJ, 283, 273
van Dijk, R., Bloemen, H., Hermsen, W., et al. 1994, in The Evolution of X-ray Binaries (New York: AIP Press), 324
Waters, L. B. F. M., Taylor, A. R., van den Heuvel, E. P. J. M., Habets, M. J. H., & Persi, P. 1988, A&A, 198, 200